Title

Time-resolved FTIR difference spectroscopy for the study of photosystem I with high potential naphthoquinones incorporated into the A1 binding site

Journal

Biochimica et Biophysica Acta (BBA) - Bioenergetics, 1864(1)

ISSN

0005-2728

Authors

Agarwala, Neva

Makita, Hiroki

Hastings, Gary

Publication Date

2023

DOI

10.1016/j.bbabio.2022.148918

Time-Resolved FTIR Difference Spectroscopy for the Study of Photosystem I with High Potential Naphthoquinones Incorporated into the A_1 Binding Site

Neva Agarwala[1], Hiroki Makita[1,#] and Gary Hastings[1,*]

[1]Department of Physics and Astronomy, Georgia State University, Atlanta, GA USA

KEYWORDS

Photosynthesis, Photosystem I, Naphthoquinone, Phylloquinone, Time-resolved step-scan FTIR, A_1, Electron Transfer

[#]Current Address: Molecular Biophysics and Integrated Bioimaging Division, Lawrence Berkeley National Laboratory, Berkeley CA 94720, USA

*Corresponding Author: e-mail: ghastings@gsu.edu, tel.: 404-413-6055

ABSTRACT

Time–resolved step-scan Fourier transform infrared difference spectroscopy has been used to study cyanobacterial photosystem I photosynthetic reaction centers from *Synechocystis* sp. PCC 6803 (*S6803*) with four high-potential, 1,4-naphthoquinones incorporated into the A_1 binding site. The high-potential naphthoquinones are 2-chloro-, 2-bromo-, 2,3-dichloro- and 2,3-dibromo-1,4-naphthoquinone. "Foreign minus native" double difference spectra (DDS) were constructed by subtracting difference spectra for native photosystem I (with phylloquinone in the A_1 binding site) from corresponding spectra obtained using photosystem I with the different quinones incorporated. To help assess and assign bands in the difference and double difference spectra, density functional theory based vibrational frequency calculations for the different quinones in solvent, or in the presence of a single asymmetric H–bond to either a water molecule or a peptide backbone NH group, were undertaken. Calculated and experimental spectra agree best for the peptide backbone asymmetrically H–bonded system. By comparing multiple sets of double difference spectra, several new bands for the native quinone (phylloquinone) are identified. By comparing calculated and experimental spectra we conclude that the mono-substituted halogenated NQs can occupy the binding site in either of two different orientations, with the chlorine or bromine atom being either ortho or meta to the H-bonded C=O group.

1. INTRODUCTION

In oxygen-evolving photosynthetic organisms, solar energy conversion takes place in two large membrane–spanning protein complexes called photosystem I and II (PSI and PSII)[1] [1]. In both photosystems, the fundamental mechanism of solar energy conversion is light–induced electron transfer (ET) across the thylakoid membrane. In both photosystems, the ET processes exhibit a remarkably high quantum efficiency [2, 3].

ET occurs in a centralized pigment–protein complex called a reaction center (RC). The organization of the ET cofactors in the PSI RC are outlined in Fig. 1. The cofactors that participate in ET are termed P700, A_0, A_1, F_X, F_A, and F_B [4]. P700 is a heterodimeric chlorophyll–*a*/ chlorophyll–*a'* (Chl–*a*/Chl–*a*') species. Chl–*a*' is a 13^2 epimer of Chl–*a* [5]. A_0 is a monomeric Chl–*a* molecule. In PSI, the secondary electron acceptor, A_1, is a phylloquinone molecule (PhQ, 2–methyl–3-phytyl–NQ). F_X, F_A, and F_B are iron sulfur [4Fe–4S] clusters. In PSI, the cofactors are arranged two near symmetrical "branches" termed the A– and B–branches. The cofactors on either branch are indicated by a subscript in Fig. 1A (e.g. A_{1A}/A_{1B}). In native PSI, following light excitation, an electron is transferred forming the secondary radical pair state, $P700^+A_1^-$ within ~50 picoseconds (ps) [6, 7]. $P700^+A_1^-$ undergoes forward ET to form $P700^+F_X^-$ in ~20 and ~300 nanoseconds (ns) at room temperature (RT, ~293 K). These time constants are thought to represent intrinsic lifetimes of ET on the B and A branches, respectively [8, 9]. Forward ET from F_X^- to the terminal electron acceptors, F_A and F_B occurs on a sub–µs timescale [10]. In isolated cyanobacterial PSI particles, the $P700^+F_{A/B}^-$ terminal radical pair state recombines, *via* repopulation of A_{1A}^- with a time constant of ~50–100 ms [11-16].

At 77 K, ET in PSI becomes heterogeneous. $P700^+A_1^-$ charge recombination occurs in ~35 % of the PSI particles, while ~20 % undergoes $P700^+F_X^-$ charge recombination [17, 18]. Both recombination reactions occur almost exclusively through A_{1A} [19]. In the remainder of the PSI particles $P700^+F_{A/B}^-$ formation is irreversible, resulting in a loss of signal amplitude in repetitive flash experiments [17, 18]. At 77 K, in native cyanobacterial PSI, the $P700^+A_{1A}^-$ state

[1] **Abbreviations:** 2BrNQ, 2–bromo–NQ; Br_2NQ, 2,3–dibromo–NQ; Cl_2NQ, 2,3–dichloro–NQ; 2ClNQ, 2–chloro–NQ; C=O, carbonyl; Chl *a*, chlorophyll *a*; DAS, decay associated spectrum; DMNQ, 2,3–dimethyl–NQ; DDS, double difference spectrum; DFT, density functional theory; DS, difference spectra/spectrum/spectroscopy; ET, electron transfer; FTIR, Fourier transform infrared; H–bond, hydrogen bond; 2MNQ, 2–methyl–NQ; NQ, 1,4–naphthoquinone; PhQ, phylloquinone (2–methyl–3–phytyl–NQ); PQ, plastoquinone–9; PSI, photosystem I; PSII, photosystem II; RC, reaction center; RT, room temperature (293 K); *S*6803, *Synechocystis* sp. PCC 6803; THF, tetrahydrofuran; TRSS, time–resolved step–scan; WT, wild type.

recombines with a time constant of ~350 μs [17, 20]. For PSI with low potential NQs incorporated $P700^+A_{1A}^-$ recombines (at 77 K) in less than 100 μs [16, 18].

Fig. 1B shows the structure of PhQ in the A_{1A} binding site, derived from the 2.5 Å X–ray crystal structure of cyanobacterial PSI isolated from *Thermosynechococus elongatus (T. elongatus)* (PDB 1JB0 [5]). Similar structures are obtained from plant and algae PSI [4, 21-24]. Neutral PhQ in PSI is asymmetrically hydrogen bonded (H-bonded) to the backbone N–H group of LeuA722. H–bonding is to the C_4=O carbonyl group that is adjacent (ortho) to the phytyl chain. The N···O distance is 2.67 Å. Electron paramagnetic resonance (EPR) data supports this asymmetric H–bonding idea for the semiquinone anion [25], as do FTIR studies [26]. The FTIR studies suggest that this H–bond is especially strong, at least for PhQ^- [26]. In spite of this, many of the underlying PhQ pigment–protein interactions, including the exact role of this asymmetric H–bonding are still not well understood [27].

To investigate the molecular properties of PhQ in the A_1 binding site in PSI (and for quinones in protein binding sites in general) one possible way is to study PSI where the native quinone is replaced with a foreign one. This process of foreign quinone incorporation has been simplified with the generation of so–called *menB*$^-$ mutant cells where PhQ biosynthesis has been disrupted. In this study, we used cyanobacterial cells from *Synechocystis* sp. PCC 6803 (*S6803*) in which the *menB* gene is inactivated. In these mutant cells a plastoquinone (PQ) molecule is recruited into the A_1 binding site instead of PhQ [28]. PQ is weakly bound and is easily displaced by incubating PSI particles in the presence of a large molar excess of different NQs [16, 25, 29], including the high potential NQs that are the subject of the current study. This is an ideal minimally disruptive incorporation method and *menB*$^-$ PSI samples with different quinones incorporated have been used in a number of spectroscopic studies [25, 26, 30-35]. These studies have shown that for all non–native incorporated quinones the position and orientation of the C=O groups is essentially the same as it is for PhQ [26].

Recent time resolved step scan (TRSS) FTIR difference spectroscopy (DS) studies of PSI with foreign quinones incorporated, together with QM/MM vibrational frequency calculations have allowed a more detailed understanding of the vibrational properties of quinones in the A_1 binding site in both the neutral and reduced states [26, 36, 37]. One suggestion from these studies is that asymmetric H–bonding to the C_4=O of PhQ is stronger in the anion state compared to the neutral state [26].

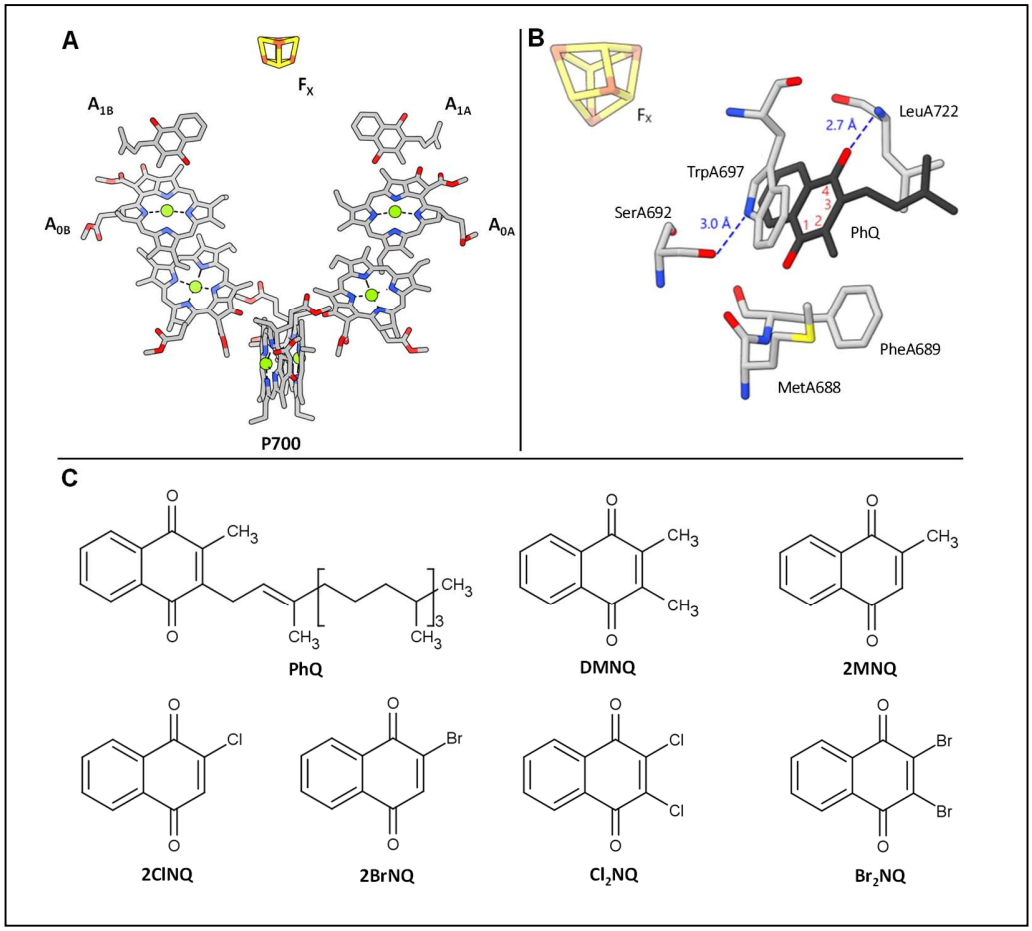

Figure 1: (A) Arrangement of ET cofactors in PSI. Structure derived from the 2.5 Å X–ray crystal structure of PSI from *T. elongatus* (PDB file 1JB0 [5]). Subscripts A and B refer to the ET branch. (B) View of PhQ in the A_{1A} binding site. Possible H–bonding interactions are indicated (*dotted*). The numbering scheme for quinonic part of the NQ ring is indicated in *red*. Atom coloring: *black*: carbon atoms of PhQ. Hydrocarbon chain of PhQ and Chl molecules are truncated for clarity in A and B. (C) Structure of the different quinones considered in this manuscript.

Most of the previous FTIR studies focused on the vibrational properties of (relatively) low potential NQs incorporated into PSI. In this manuscript we focus on studies of PSI with a series of high potential halogenated NQs incorporated. There are many reasons for this, one of them being that it is, or will be, possible to study PSI at RT, as microsecond $P700^+A_1^-$ recombination is still the dominant decay pathway at RT in PSI with high potential NQs incorporated [18]. In preparation for these future TRSS FTIR studies we first present here studies at 77 K, focusing on the quinones in the reduced states [30, 36, 38-40].

In this manuscript, we probe the vibrational properties of four different high potential NQs incorporated into the A_1 protein binding site by obtaining [$P700^+A_1^-$ – $P700A_1$] and [A_1^- – A_1] FTIR DS and "foreign – native" DDS. We show that bands in the DS are unmasked and more easily visualized when multiple DDS can be compared. To aid in spectral interpretation of the demasked bands we also used DFT based vibrational frequency calculations for the different quinones in solvent or in the presence of a single asymmetric H–bond.

2. MATERIALS AND METHODS

Quinones and solvents were obtained from Sigma–Aldrich Inc. (St Louis, MO), and used as received. 2ClNQ was obtained from Pure–Chemistry Scientific (Burlington, MA) and was used as received.

Trimeric PSI particles isolated from *menB*$^-$ mutant cells from *Synechocystis* sp. PCC 6803 (*S6803*) were prepared as described previously [28]. Quinones were introduced into the A_1 binding site by incubating PSI samples in the presence of the quinone of interest. The PSI particle to quinone ratio was approximately 1:500. Quinones were dissolved in dimethyl sulfoxide (DMSO) and added to a suspension of PSI particles in such a way that the volume of the solvent in the mixture never exceeds 2% of the total volume. Incubation periods of 12–24 hrs. at room temperature (RT, 293 K), with stirring, were typically used.

Following incubation, PSI samples were resuspended in Tris buffer (50 mM Tris buffer with 0.04% n–dodecyl–β–D-maltoside (β–DM)) at pH 8 to make total volume of 1 mL, and then centrifuged at 408,000 g for ~3 hours to produce a soft pellet. Phenazine methosulfate (PMS) (20 μM) and sodium ascorbate (20 mM) were added to the soft pellet (0.1 μL each), which was then squeezed between two circular calcium fluoride (CaF_2) windows. The sample thickness was adjusted so that the optical density of the amide I band (at ~1656 cm^{-1}) was between 0.6 and 1.0. The CaF_2 windows were sealed with vacuum grease and placed in a custom sample holder for measurements at RT. For measurements at low temperature (LT, 77 K) the sample was loaded into a liquid nitrogen cooled cryostat (Cryo Industries of America Inc., Manchester, NH).

FTIR absorption spectra of the different NQs were measured using a Varian 600 UMA FTIR microscope (Varian Inc., MA, USA), utilizing a mercury cadmium telluride (MCT) detector. Spectra were collected at 4 cm^{-1} resolution. Peak positions reported here are accurate to roughly ± 1 cm^{-1}. The different NQs were dissolved in tetrahydrofuran (THF) at various concentrations,

and a small drop (<5 μL) was deposited on a zinc selenide window. An FTIR spectrum of pure THF was also obtained and interactively subtracted from the quinone spectrum.

Static, photo–accumulated [$P700^+ - P700$] FTIR DS were obtained at 77K as described previously using a Bruker Vertex80 FTIR spectrometer equipped with a MCT detector (Bruker Optics, Billerica, MA) [41-44]. Illumination was provided by a 20-mW helium neon laser, expanded to a spot size of ~1 cm at the sample.

Time–resolved step–scan (TRSS) FTIR DS were collected in a manner similar to that described previously [42-45], using the same Bruker Vertex 80 FTIR spectrometer equipped with a MCT detector. TRSS FTIR DS were collected with 6 μs time resolution over a 3.5 ms time window at 77 K. Data were collected at 4 cm^{-1} spectral resolution in the 1950–1100 cm^{-1} region. Light above 1950 cm^{-1} was blocked by placing 2000–1000 cm^{-1} bandpass filters both before the sample and in front of the MCT detector. The latter also blocks stray laser illumination from reaching the detector. Light below ~1100 cm^{-1} was also blocked by the CaF_2 sample windows, and the windows on the cryostat shroud. Sample excitation was provided by 532 nm laser flash of 5 ns duration from a Minilite Nd:YAG laser (Continuum, San Jose, CA) operating at 10 Hz. Laser flashes with a power of ~0.785 mJ/cm^2 (1 mJ per pulse spread over a circle of diameter of ~1 cm at the sample) were used. TRSS FTIR DS measurements were repeated ~40 times for each PSI sample. At least three independently prepared PSI samples (with the different quinones incorporated) were used, and the result of ~120 full step-scan acquisitions were averaged. The standard error of the three independent spectra obtained for each sample is taken as a measure of experimental variability (noise level) in the measurements and is indicated as error bars on the spectra.

The complete TRSS FTIR DS data set was globally analyzed using Glotaran software [46]. The TRSS FTIR DS were fitted globally to multi–exponential functions and decay–associated spectra (DAS) were constructed. This was done in part to separate spectral features associated with a sample heating artifact caused by the actinic laser flashes used to initiate photochemistry [26].

DFT–based molecular geometry optimization and harmonic normal–mode vibrational frequency calculations were undertaken as described previously [47], using Gaussian16 software (Gaussian Inc. Wallingford, CT) [48]. The phytyl tail of PhQ was truncated to a 5–carbon unit [$CH_2CHC(CH_3)_2$]. Asymmetric H–bonded quinone models were constructed starting from the

2.5 Å X–ray crystal structure of PSI from *T. elongatus*. To construct this model for the other NQs, PhQ in the A_{1A} binding site was modified without altering the position and orientation of the quinonic ring atoms.

DFT calculations were performed using the B3LYP functional in combination with the 6–31+G(d) basis set [49]. For the anion state of the quinone of interest, the overall charge was assigned as –1. The solvent (THF) was considered using the integral equation formalism of the polarizable continuum model [50] using default parameters in Gaussian16 software. Harmonic, normal mode vibrational frequency calculations result in "stick spectra" (intensities at given frequencies). These stick spectra are convolved with Gaussian functions of 4 cm^{-1} half–width, to produce more realistic looking absorption spectra.

For each molecular model a single scaling factor was calculated by taking the ratio of the calculated and experimental frequencies of the main $C_1{=}O$ mode of PhQ^- (at 1495 cm^{-1} [26]). These scaling factors are purely for ease of comparison and are largely irrelevant as it is primarily the shift in the vibrational frequencies for the different quinones that are of interest, and this shift does not depend significantly on the scaling factor.

An assignment of calculated frequencies to molecular groups was based on visual inspection of the calculated atomic displacements associated with the normal modes. The atomic displacements were visualized using GaussView 6 software (Gaussian, Wallingford, CT).

For isolated quinones in solution, potential energy distributions (PEDs) associated with the normal modes are calculated using VEDA [51]. PEDs provide a percentage estimate of how much a specific molecular group contributes to a normal mode.

3 RESULTS

3.1 TRSS FTIR DS and DDS for PSI with different NQs incorporated

As described previously, PSI samples were prepared for FTIR DS measurements and immediately frozen to 77 K in the dark [52]. FTIR DS for PSI with different halogenated NQs incorporated have not been presented previously, and a paper discussing both the neutral and anion region would become unmanageable. For this reason, we focus here on spectral features in the ~1540–1400 cm^{-1} semiquinone anion spectral region and will defer studies in other spectral regions to another manuscript.

From global analysis of the 77 K TRSS FTIR DS data sets, major decay phases with lifetime of 366/391/239/114/94/78/70 µs were found for PSI with PhQ/DMNQ/2MNQ/2ClNQ/2BrNQ/

Cl_2NQ/Br_2NQ incorporated, respectively. Lifetimes for PSI with the different quinones incorporated were presented previously [16, 20, 32].

The spectra associated with these lifetimes are called decay associated spectra (DAS), and Fig. 2 shows DAS for PSI samples with the different quinones incorporated. These DAS correspond to radical pair recombination at 77K and are therefore called [$P700^+A_1^-$ – $P700A_1$] FTIR DAS. In the FTIR DAS in Fig. 2 bands are due to $P700^+/P700$, A_1^-/A_1, and protein modes, which are impacted by $P700^+A_1^-$ radical pair formation. A photoaccumulated [$P700^+$ – P700] FTIR DS in the anion region is also shown in Fig. 2A.

Prominent positive bands are observed in the [$P700^+A_1^-$ – $P700A_1$] FTIR DAS that are not observed in [$P700^+$ – P700] FTIR DS. These positive bands are attributed mainly to vibrational modes of the semiquinone anion in the A_1 binding site. For example, positive bands at 1495 and 1415 cm^{-1} in [$P700^+A_1^-$ – $P700A_1$] FTIR DAS for PSI with PhQ incorporated (native PSI) have previously been shown to be due to $C_1{=}O$ and $C_4{=}O$ stretching vibrations of PhQ^- [26]. In [$P700^+A_1^-$ – $P700A_1$] FTIR DAS for PSI with 2MNQ incorporated positive bands are observed at 1506 and ~1432 cm^{-1} and these bands have also previously been shown to be partly due to the $C_1{=}O$ and $C_4{=}O$ stretching vibrations of $2MNQ^-$ [26, 53].

[$P700^+A_1^-$ – $P700A_1$] FTIR DAS contain contributions from multiple species. Often these species display difference features that are considerably more intense than the features (of the quinones) that are of interest. To focus on the analysis of bands associated with the semiquinones often [$P700^+$ – P700] FTIR DS are subtracted from [$P700^+A_1^-$ – $P700A_1$] FTIR DAS to produce a so–called [A_1^- – A_1] FTIR DS. Fig. 3 shows [A_1^- – A_1] FTIR DS obtained using PSI with the different quinones incorporated.

[A_1^- – A_1] FTIR DS are relatively free of contributions from $P700/P700^+$ but still contain contributions from protein modes that are impacted by A_1^- formation. To focus on bands associated with the quinones, DDS can be constructed by taking the difference between [A_1^- – A_1] FTIR DS obtained using PSI with two different quinones incorporated. An alternative would be to take the difference between [$P700^+A_1^-$ – $P700A_1$] DAS obtained using PSI with two different quinones incorporated [26, 54]. This latter approach does not require the separate collection of photoaccumulated [$P700^+$ – P700] FTIR DS and is usually preferable, although we do find that [$P700^+$ – P700] FTIR DS are near identical for PSI samples with different quinones incorporated. Here we focus on DDS calculated by subtracting the [$P700^+A_1^-$ – $P700A_1$] FTIR

DAS for PSI with PhQ incorporated from all the other DAS for PSI with the different quinones incorporated. These DDS could be called “foreign minus native” DDS. Fig. 4 shows several “foreign minus native” DDS. In these DDS bands associated with PhQ^- are negative. Since [$P700^+A_1^-$ – $P700A_1$] FTIR DAS for PSI with PhQ incorporated were used to construct all the DDS in Fig. 4, negative bands of PhQ^- should be present in all the DDS. Negative bands are observed at 1494 and 1414 cm^{-1} in the DDS in Fig. 4 (B, C, D), and so these bands are due to PhQ^-. The 1494 cm^{-1} band is not so clear in Fig. 4A, E and F. This may be due to both quinones having bands at similar frequencies.

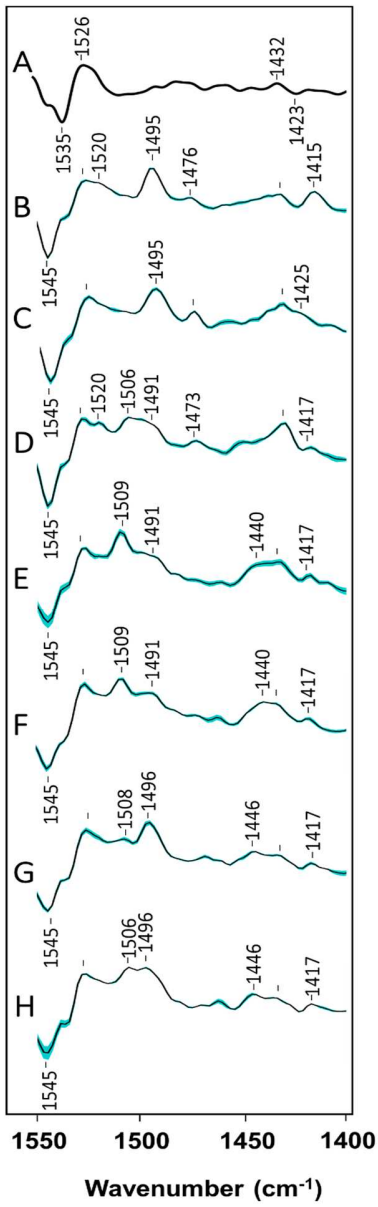

Figure 2: Photoaccumulated [$P700^+ - P700$] FTIR DS (A) and [$P700^+A_1^- - P700A_1$] FTIR DAS (B–H) in the 1550–1400 cm^{-1} regions obtained at 77 K using PSI particles with (B) PhQ, (C) DMNQ, (D) 2MNQ, (E) 2ClNQ, (F) 2BrNQ, (G) Cl_2NQ and (H) Br_2NQ incorporated. Spectra are normalized to the ~1718/1697 cm^{-1} difference band. Spectra shown are the average of at least 3 separate experiments. The standard error derived from these separate measurements are also shown (*blue shade*). Photoaccumulated DS have been shown to be nearly identical for PSI with different quinones incorporated. The photoaccumulated DS shown here is the average from over fifty independent PSI samples with different quinones incorporated.

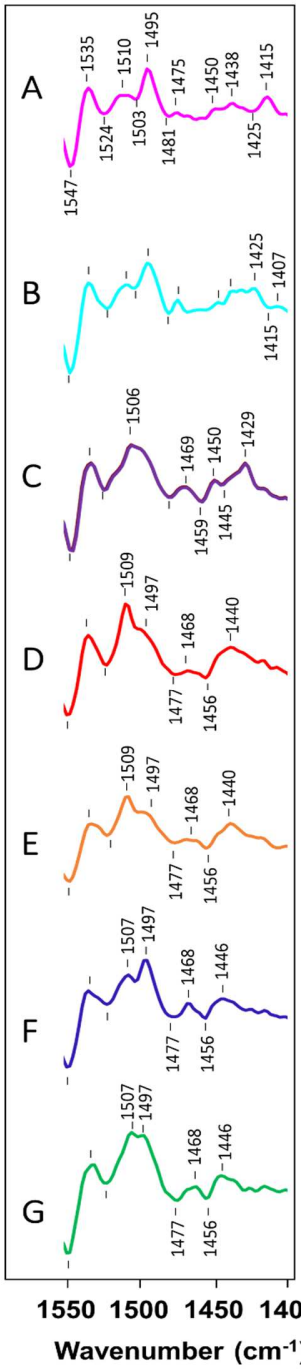

Fig. 3: [$A_1^- - A_1$] FTIR DS in the 1550–1400 cm^{-1} region, obtained at 77 K for *menB*⁻ PSI particles with (A) PhQ, (B) DMNQ, (C) 2MNQ, (D) 2ClNQ, (E) 2BrNQ, (F) Cl_2NQ, and (G) Br_2NQ incorporated into the A_1 binding site.

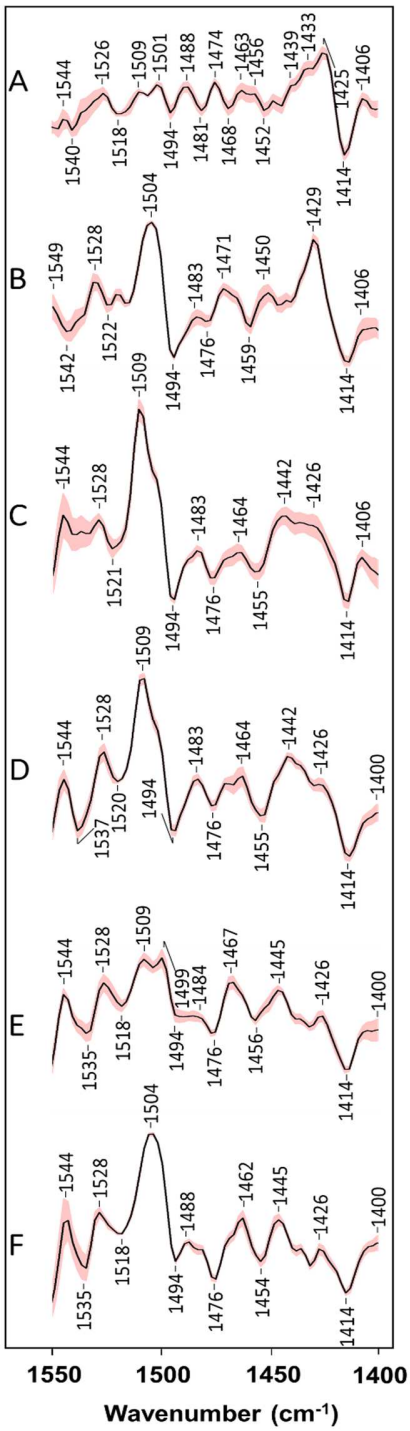

Figure 4: Double difference spectra (DDS) in the 1550–1400 cm^{-1} region constructed by subtracting the [$P700^{+}A_1^{-}$ – $P700A_1$] DAS for native PSI from the corresponding DAS for PSI with the indicated quinone incorporated. (A) (DMNQ – PhQ), (B) (2MNQ – PhQ), (C) (2ClNQ – PhQ), (D) (2BrNQ – PhQ), (E) (Cl_2NQ – PhQ) and (F) (Br_2NQ – PhQ). The propagated standard error is shown (*red shade*).

3.2 DFT calculated FTIR absorption spectra of NQs

To aid in the analysis and interpretation of the bands in the DS and DDS we have undertaken DFT–based harmonic, normal–mode vibrational frequency calculations for the different semiquinone anions in THF (Fig. S1). We have also undertaken calculations for the semiquinones H–bonded to either a water molecule (Fig. S2) or to the amide backbone N–H group of a Leu residue (Fig. 5/S3). The different molecular models are referred to as follows: (Q^{-}+H_2O) for the semiquinones H-bonded to a water molecule; (Q^{-}+Leu) for the model shown in the inset in Fig. 5 for the semiquinones H-bonded to a peptide N–H group of a truncated Leu residue. The inset in Fig. 5 indicates the molecular model also includes a portion of the backbone from Ala721 and Ser723. When necessary, we will refer to this as (Q^{-}+Leu, model 1 (m_1)). A slightly simpler model with a reduced number of atoms in the protein backbone is considered in Fig S3. When necessary, we will refer to this simpler model as (Q^{-}+Leu, model 2 (m_2)). Comparison of the data in Fig. 5 and S3-S7 indicate very similar spectra are calculated for the m_1 and m_2 models.

A model termed (flipped Q^{-}+Leu (f-m_1)) is also considered, where the semiquinone is rotated ~180^{o} along the axis perpendicular to the line joining the C=O groups (quinone is "flipped"). For the three mono substituted NQs, the quinones are "flipped" simply by interchanging the positions of groups attached at C_2 and C_3. Calculated spectra for the "flipped" monosubstituted NQs are shown as *dotted* lines in Fig. 5 and S3. Composite spectra that are the average of the spectra obtained using the flipped and non-flipped models are also shown in Fig. 5 (*grey dotted lines*).

In this study, for PSI with non-native NQs incorporated, we will refer to the H–bonded C=O group as the C_4=O group. We will also refer to the substitutions at C_3 and C_2 as being ortho or meta to the H–bonded C_4=O group, respectively. In some instances, this numbering scheme is not in keeping with IUPAC numbering, but it will make it simpler to compare normal modes for the different incorporated NQs.

Molecular groups that contribute to the bands in the various calculated spectra are listed in Table S1/S2/S3. The calculated frequencies, intensities, and assignments of the $C_1{=}O$ and $C_4{=}O$ vibrational modes of the semiquinones for the different models are listed in Table S4. Key bond lengths and angles obtained from the calculated optimized geometries of the different quinones are listed in Table S5.

Fig. 6 shows the calculated DDS obtained using the spectra in Fig. 5. Comparison of calculated DDS obtained using the flipped and non-flipped models, for the monosubstituted NQs, are shown in Fig. 7. The average of the two DDS for the flipped and non-flipped models are also shown in Fig. 7. The spectra in Fig. 7 are obtained using the (Q^{-}+Leu, model 1), but very similar results are obtained using the slightly simpler (Q^{-} + Leu, model 2) (Fig. S4/S5/S6/S7).

Note that for PhQ^{-}, the main C⩶O bands are calculated at 1495 and 1428 cm^{-1}. Experimentally, the bands are at 1494 and 1414 cm^{-1}. So, it may be appropriate to use a separate set of scaling factors for the different spectral regions, but this will not be implemented in this manuscript.

Fig. S8 shows a model indicating the calculated bond lengths and angles for reduced PhQ^{-} obtained using the different models. The various bond lengths and angles for the different models are listed in Table S5.

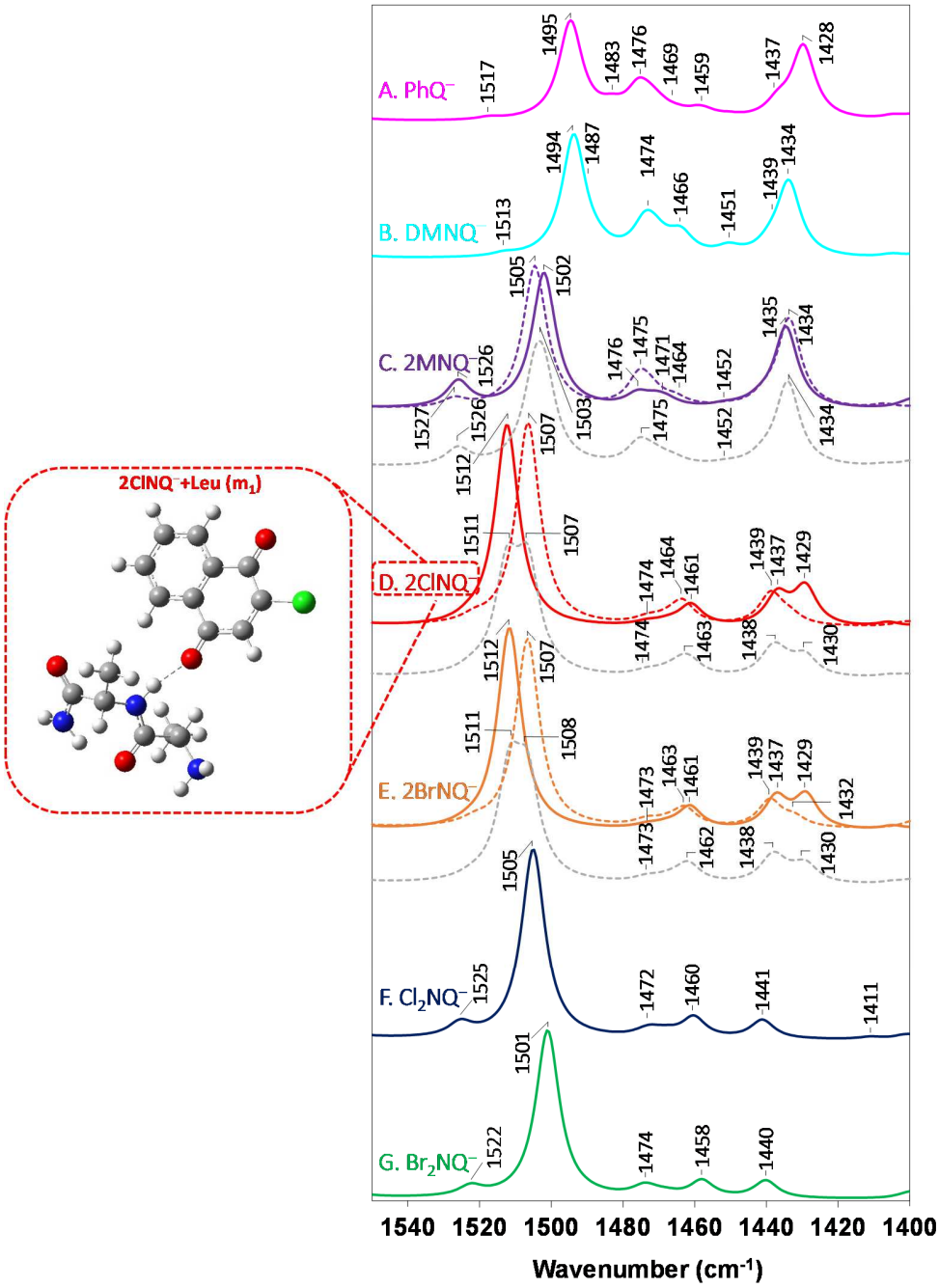

Figure 5: Calculated spectra for the semiquinones where the C_4=O group is H–bonded to the backbone of a truncated Leu residue (see *inset*). (A) PhQ^-, (B) $DMNQ^-$, (C) $2MNQ^-$, (D) $2ClNQ^-$, (E) $2BrNQ^-$, (F) Cl_2NQ^- and (G) Br_2NQ^-. Calculated frequencies are scaled by 0.971. For the monosubstituted NQs, the appropriately color-coded dotted lines show the spectra calculated when the semiquinone is "flipped". The grey dotted lines show the average of the spectra obtained using the flipped and non-flipped models.

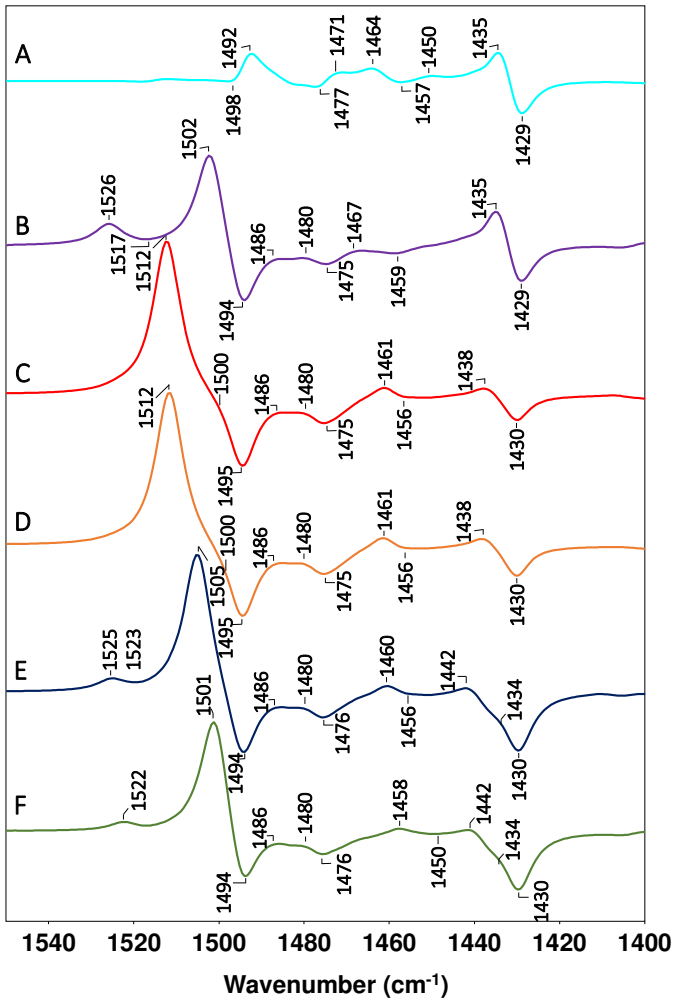

Figure 6: Double difference spectra (DDS) constructed using the spectra obtained using the "non-flipped" models in Fig. 5. (A) (DMNQ – PhQ), (B) (2MNQ – PhQ), (C) (2ClNQ – PhQ), (D) (2BrNQ – PhQ), (E) (Cl_2NQ – PhQ) and (F) (Br_2NQ – PhQ).

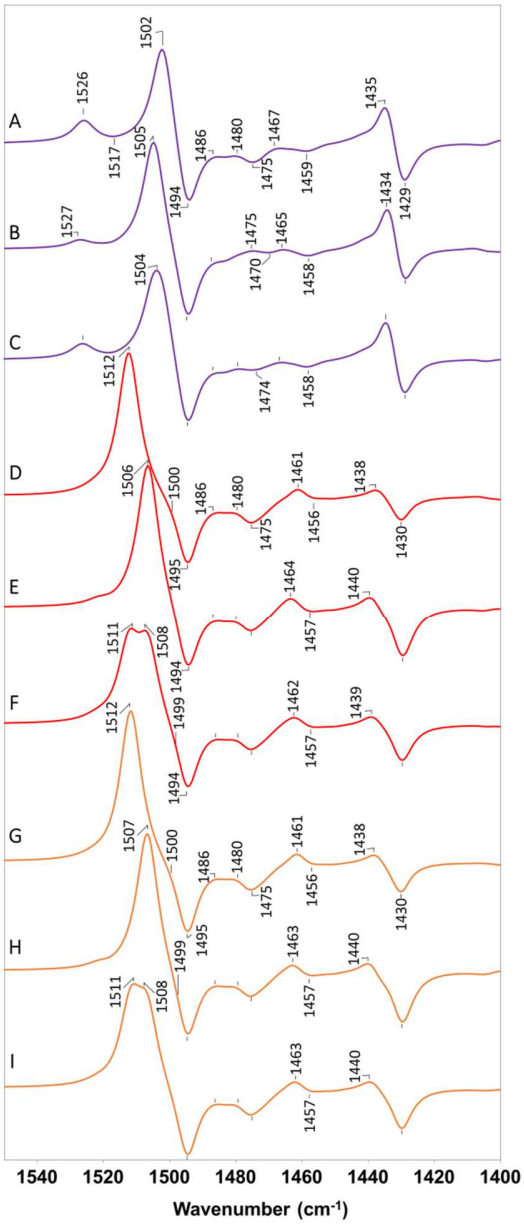

Figure 7: DDS constructed using the spectra in Fig. 5. Spectra in A-C are for (2MNQ – PhQ) for the (A) non-flipped model, (B) flipped model and (C) the average of the spectra in A and B. Spectra D-F are for (2ClNQ – PhQ) for the (D) non-flipped model, (E) flipped model, and (F) the average of the spectra in D and E. Spectra G-I are for (2BrNQ – PhQ) for the (G) non-flipped model, (H) flipped model, and (I) the average of the spectra in D and E.

4 DISCUSSION

4.1 Experimentally observed semiquinone bands

Intense IR bands due to the C⩶O modes of the semiquinone anions are found in the ~1550−1400 cm^{-1} region. Spectral contributions from $P700^+$/P700 and other protein modes are weak in this region (Fig. 2A) and bands associated with the bound quinone may be more easily visualized (Fig. 2B-H). Despite this, bands associated with the bound quinone are best visualized in the DDS (Fig. 4). For all DDS shown in Fig. 4, FTIR DS obtained using native PSI with PhQ incorporated have been subtracted. Since quinone anion bands are positive in this region, negative bands that appear in the DDS are due to PhQ^-. Off course, bands that appear at a similar frequency in both native PSI and PSI with a foreign quinone incorporated will not show up in the DDS. For example, in the DS for PSI with $DMNQ^-$ or PhQ^- incorporated, a band is observed near 1494 cm^{-1} (compare Fig. 3A and B). Consequently, no negative feature is observed near 1494 cm^{-1} in the (DMNQ – PhQ) DDS (Fig. 4A).

The DDS in Fig. 4B−F clearly indicate (negative) PhQ^- bands at 1494 and 1414 cm^{-1}. These bands are due mainly to C_1⩶O and C_4⩶O stretching vibrations of PhQ^- [26, 39, 53]. The separation between the two C⩶O modes is 80 cm^{-1}, which may in part be due to (relatively) strong H−bonding to the C_4=O group *in the anion state*. [Note that it is probably unwise to make the statement that the 1414 cm^{-1} band is due to a C_4⩶O stretching vibration. More accurately, the band is due to a normal mode that contains contributions from several molecular groups, only one of which is the C_4=O group]. Recently it has been suggested for neutral PhQ in PSI that the C_1=O and C_4=O modes are separated by ~30 cm^{-1} [39]. So, one might argue that H−bonding is strengthened upon anion formation. It is difficult to imagine structural or bioenergetic benefits that could arise from this anion induced H-bond strengthening. For example, Srinivasan et al. have indicated that PhQ retains its native orientation even in mutant PSI samples where H−bonding to PhQ has been altered [55]. Furthermore, H−bonding is expected to stabilize the semiquinone, leading to a higher (more positive) midpoint potential of PhQ [55, 56] [57, 58]. So, anion induced H−bond strengthening might be expected to be disadvantageous for ET in PSI, which requires the A_1 pigment to operate at a highly negative redox potential.

For PSI with DMNQ incorporated, the semiquinone C⩶O modes give rise to bands at 1495 and ~1432 cm^{-1} (Fig. 2C). For PSI with 2MNQ incorporated the semiquinone C⩶O modes give rise to bands at 1506 and 1432 cm^{-1} (Fig. 2D). For PSI with 2ClNQ and 2BrNQ incorporated, the

$C_1{=}O$ mode gives a very intense band at 1509 cm^{-1} in the DDS, while there appear to be two features at ~1442 and 1426 cm^{-1} (Fig. 4C, D), either of which could correspond to the 1415 cm^{-1} band of PhQ^-. For PSI with Cl_2NQ and Br_2NQ incorporated, at least two positive bands appear in the 1509–1496 cm^{-1} range (Fig. 4E, F), either of which may correspond to the 1494 cm^{-1} band of PhQ^-. Positive bands also appear near 1445 and 1426 cm^{-1}. Again, either of these bands could correspond to the 1415 cm^{-1} band of PhQ^-. The calculations discussed below may help to address these issues.

The (2MNQ – PhQ), (2ClNQ – PhQ), (2BrNQ – PhQ), (Cl_2NQ – PhQ) and (Br_2NQ – PhQ) DDS all display prominent negative bands at 1494 and 1414 cm^{-1}. As discussed above, this confirms previous work that these bands are due to PhQ^- [26]. The observation of negative bands due to PhQ^- in the DDS indicates that corresponding modes of the non–native semiquinones are shifted relative to PhQ^- in the A_1 binding site.

Five of the DDS exhibit a negative band at 1476 cm^{-1}, which was recently assigned to a PhQ^- C–H bending mode associated with the methyl group at C_2 [29, 39]. Again, this observation from multiple DDS indicate that such a mode is shifted for PSI with foreign quinones incorporated.

Six of the DDS in Fig. 4 show negative bands (due to PhQ^-) in the 1517–1522 and 1454–1459 cm^{-1} range. Such PhQ^- features are not obvious in the [$P700^+A_1^-$ – $P700A_1$] (Fig. 2B) and [A_1^- – A_1] FTIR DS (Fig. 3A). In this manner we demonstrate the potency of using multiple different DDS to uncover "hidden" bands in FTIR DS.

In the (DMNQ – PhQ) DDS most of the features are very weak , indicating that $DMNQ^-$ gives rise to normal modes at the same frequencies to that of PhQ^-. The main difference being that the (predominantly) $C_4{=}O$ mode is upshifted ~11 cm^{-1} to 1425 cm^{-1} for $DMNQ^-$. Replacing the phytyl chain with a methyl group therefore influences predominantly the $C_4{=}O$ mode and not the $C_1{=}O$ mode, which might be expected given the proximity of the phytyl chain (at C_3) to the carbonyl group (at C_4). For $DMNQ^-$, the separation between the $C_1{=}O$ and $C_4{=}O$ modes is ~69 cm^{-1}.

In the ($2MNQ^-$ – PhQ^-) DDS in Fig. 4B intense positive bands are observed at 1504 and 1429 cm^{-1} and are assigned to (predominantly) $C_1{=}O$ and $C_4{=}O$ modes of $2MNQ^-$, respectively. These modes are therefore upshifted 10 and 15 cm^{-1}, respectively, for $2MNQ^-$ compared to PhQ^-. The mode separation is 75 cm^{-1}, close to the 80 cm^{-1} found for PhQ^-.

Previous EPR experiments [59] and recent QM/MM vibrational frequency calculations [53], have indicated that the methyl group of 2MNQ is in the same position as it is for PhQ in the A_1 binding site. Therefore, the H atom of 2MNQ is in the position normally occupied by the phytyl chain of PhQ in the A_1 binding site. That is, replacing the phytyl chain of PhQ by a methyl group or a H atom leads to a similar upshift for the $C_4{=}O$ mode. Replacing the phytyl chain by a H atom also causes an upshift of the $C_1{=}O$ mode. This is not the case for replacing the phytyl chain by a methyl group (no upshift is observed).

In *menG* mutant PSI a methyl less PhQ analogue (sometimes called demethyl PhQ) occupies the A_1 binding site. That is, the methyl group of PhQ is replaced with a H atom. In the *menG* mutant the incorporated demethyl-PhQ $C_1{=}O$ mode upshifts ~6 cm^{-1} [60].

In the (2ClNQ – PhQ) and (2BrNQ – PhQ) DDS in Fig. 4 an intense band is observed at 1509 cm^{-1},with a shoulder appearing near 1500 cm^{-1}. These two features could indicate a mix of two separately oriented NQ populations. Some with the H atom at the C_2 position and some with it at the C_3 position. If this is the case, then one might suggest that the Cl (or Br) atom does not have a particular affinity for either location (at C_2 or C_3) in the A_1 binding site. However, the positive 1509 cm^{-1} band in the DDS is more intense than this ~1500 cm^{-1} shoulder, which might indicate a population skewed in favor of one orientation over the other.

In the (2ClNQ – PhQ) and (2BrNQ – PhQ) DDS there is a positive feature at 1426 cm^{-1} that would indicate a 12 cm^{-1} upshift of the $C_4{=}O$ mode of $2ClNQ^-$ (or $2BrNQ^-$) relative to PhQ^-. This seems a reasonable upshift for an H atom at C_3, although it is not entirely clear what kind of band shifts to expect for either the $C{=}O$ mode upon incorporating a Cl atom at either the C_2 or C_3 position. In the (2ClNQ – PhQ) and (2BrNQ – PhQ) DDS there is also a positive feature at 1442 cm^{-1} that could indicate a 28 cm^{-1} upshift of the $C_4{=}O$ mode of $2ClNQ^-$ (or $2BrNQ^-$) relative to that of PhQ^-. Again, two features could indicate a mix of two separately oriented NQ populations in PSI. The calculations discussed below might help address this issue. One final point to bear in mind is that the ~1426 cm^{-1} band in the DDS in Fig. 4C, D is close to the noise level in the experiment, and it may be reasonable to refrain from attempting to assign this feature. This is not the case for the feature that appears near 1442 cm^{-1}, which is well above the noise level.

The (2MNQ – PhQ) DDS exhibits positive bands at 1528, 1483, and 1471 cm^{-1}, all of which could indicate absorption bands of $2MNQ^-$ which are upshifted ~8, 7 and 15 cm^{-1} relative to the

PhQ^- bands at ~1520, ~1476 and ~1456 cm^{-1}. Similar conclusions apply to the (2ClNQ – PhQ) and (2BrNQ – PhQ) DDS where the positive band near 1483 cm^{-1} is much clearer than in (2MNQ – PhQ) DDS. It seems also that a similar set of positive bands at 1528, 1488 and ~1462 cm^{-1} are observable in the (Cl_2NQ – PhQ) and (Br_2NQ – PhQ) DDS.

In the (Cl_2NQ – PhQ) DDS, the band associated with the $C_1{=}O$ vibration is split into two bands at 1499 and 1509 cm^{-1}. Such a splitting is probably also likely in the (Br_2NQ – PhQ) DDS, but only a single broad positive peak is observed at 1504 cm^{-1}. Both the (Cl_2NQ – PhQ) and (Br_2NQ – PhQ) DDS display a positive band at 1445 cm^{-1}, and a much weaker band at 1426 cm^{-1}. These peaks are similar to that observed in the (2ClNQ – PhQ) and (2BrNQ – PhQ) DDS and both might be assigned to a $C_4{=}O$ vibrational mode of Cl_2NQ^- (or Br_2NQ^-).

4.2 Vibrational mode frequency calculations to aid in experimental band assignments

To assign bands in the experimental spectra DFT based vibrational frequency calculations for the semiquinones were undertaken using several different molecular models. In the main manuscript we focus on the (Q^-+Leu model 1 (m_1)), which for $2ClNQ^-$ is shown in the inset of Fig. 5. Calculations were also undertaken using a model where the quinone is “flipped" (referred to as (f-m_1)). The average of the spectra obtained using the flipped and non-flipped quinone models is referred to as (avg. m_1). Calculated spectra for the Q^-+Leu (m_1) and Q^-+Leu (m_2) are shown in Fig. 5 and S3 respectively. DDS calculated using model m_1 are shown in Fig. 6.

The most intense band in the calculated spectra occurs in the 1495–1512 cm^{-1} range (Fig. 5). For PhQ^-, a vibrational mode is calculated at 1495 cm^{-1} and is due to a $C_1{=}O$ vibration with some coupling to a $C_4{=}O$ stretching and aromatic CH bending modes (see movie titled “1495 mode of PhQ^-” in the SI). The negative 1494 cm^{-1} band in the experimental DDS (Fig. 4) is also due to this mode. For $DMNQ^-$/$2MNQ^-$/$2ClNQ^-$/$2BrNQ^-$/Cl_2NQ^-/Br_2NQ^- the corresponding $C_1{=}O$ mode is calculated to be shifted –1/+7/+17/+17/+10/+6 cm^{-1}, respectively (Fig. 5). These shifts compare favorably to the experimentally observed shifts of 0/+10/+15/+15/+5–15/+10 cm^{-1} (Fig. 4). The trend in the frequency of the $C_1{=}O$ mode observed experimentally for different quinones in PSI is captured well in the calculated data. This trend is also well captured using the Q^-+Leu (m_2) model (0/+9/+19/+18/+14/+14 cm^{-1}) (Fig. S3), the Q^-+H_2O model (0/10/20/20/17/17 cm^{-1}) (Fig. S2), and for calculations of the semiquinones in THF (0/10/15/16/14/14 cm^{-1}) (Fig. S1). So how the calculated $C_1{=}O$ mode frequencies shift for the

different incorporated semiquinones is not a particular valuable probe for assessing which of the molecular models is most appropriate.

The 1494 cm^{-1} band of PhQ^- is clearly visible as a negative band in all the calculated DDS in Fig. 6, except for $DMNQ^-$, which has a band at similar frequency to that of PhQ^-.

In the Q^-+Leu (m_1) model for the monosubstituted NQs, $2MNQ^-$/$2ClNQ^-$/$2BrNQ^-$, as mentioned above the $C_1{=}O$ mode is calculated to be shifted +8/+17/+17 cm^{-1} relative to that of PhQ^-, respectively (Fig. 7A, D, G). When these monosubstituted NQs are flipped, however, the $C_1{=}O$ mode of $2MNQ^-$/$2ClNQ^-$/$2BrNQ^-$ is shifted +10/+12/+12 cm^{-1} relative to that of PhQ^-, respectively (Fig. 7B, E, H). Upon averaging the DDS for the flipped and non-flipped models for the monosubstituted NQs, the $C_1{=}O$ mode for $2MNQ^-$ is upshifted 10 cm^{-1} (Fig. 7C). For $2ClNQ^-$ the $C_1{=}O$ band is split into two with peaks at 1511 and 1508 cm^{-1} (upshifted 16 and 13 cm^{-1} relative to that of PhQ^-) (Fig. 7F). Similar results are found in the averaged (2BrNQ - PhQ) DDS (Fig. 7I). This splitting of the $C_1{=}O$ mode observed in the average calculated (2ClNQ – PhQ) and (2BrNQ – PhQ) DDS is in line with that observed in the experimental DDS (Fig. 5), although experimentally the splitting is more asymmetric with the higher frequency peak being more intense. For the averaged calculated (2MNQ – PhQ) DDS (Fig. 7C) a splitting of the positive band (at 1504 cm^{-1}) is less obvious, although in the experimental DDS this positive feature is quite broad (Fig. 5C), as it is in the calculated DDS.

Since the average calculated DDS for the monosubstituted NQs are more in line with experiment the suggestion is that the monosubstituted NQs, particularly 2ClNQ and 2BrNQ, are incorporated into the A_1 binding site in both the flipped and non-flipped orientations. This conclusion follows from only a consideration of bands associated with the $C_1{=}O$ modes. Note that the orientation of $2MNQ^-$ in the A_1 binding site has been established using higher-level ONIOM type QM/MM vibrational frequency calculations [61], and a similar set of calculations for $2ClNQ^-$ and $2BrNQ^-$ incorporated into PSI will be undertaken in the near future.

In the Q^-+Leu (m_1) model for PhQ^- there are several modes that contain a contribution from the $C_4{=}O$ stretching vibration. The most intense predominantly $C_4{=}O$ mode is calculated at 1428 cm^{-1} (see movie titled "1428 mode of PhQ^-" in the SI). The calculated separation of the $C_1{=}O$ and $C_4{=}O$ modes of PhQ^- is therefore 67 cm^{-1}. This result is more in line with experiment (80 cm^{-1}) than the separation predicted by the Q^-+H_2O model (59 cm^{-1}) (Fig S2 and Table S2). As

discussed above, the fact that the $C_4{=}O$ mode of PhQ^- is calculated to be at 1428 cm^{-1} (and not 1414 cm^{-1}) poses some problems for a direct comparison of calculated and experimental DDS. Notwithstanding this issue, it may still be reasonable to calculate frequency shifts for corresponding modes of the different NQs.

For $DMNQ^-$/$2MNQ^-$/$2ClNQ^-$/$2BrNQ^-$/Cl_2NQ^-/Br_2NQ^- the corresponding $C_4{=}O$ mode is calculated at 1434/1435/1429/1429/1441/1440 cm^{-1} and is therefore shifted +6/+7/+1/+1/+13/+12 cm^{-1}, respectively, relative to the PhQ^- mode (Fig. 5). These results do not agree with the experimentally observed shifts of +11/+15/+12/+12/+31/+30 cm^{-1} (Fig. 4). A similar conclusion applies to data calculated using the Q^-+Leu (m_2) model (+2/+3/–1//–1/+8/+9 cm^{-1}) (Fig. S3).

The ~1429 cm^{-1} calculated band of PhQ^- is observed as a negative band in all the calculated DDS in Fig. 6. So, this mode is clearly shifted for all the NQs relative to PhQ. The 1414 cm^{-1} band of PhQ^- is also observed as a negative feature in all the experimental DDS (Fig. 5), so for this particular type of comparison the calculated and experimental DDS agree well.

In the DDS for the monosubstituted NQs, $2MNQ^-$/$2ClNQ^-$/$2BrNQ^-$, in the Q^-+Leu (m_1) model (Fig. 7A, D, F) the $C_4{=}O$ mode is calculated to upshift +6/+8/+8 cm^{-1} relative to PhQ^- (which is at 1429-1430 cm^{-1}), respectively. If the monosubstituted NQs are flipped, however, the $C_4{=}O$ mode is upshifted +6/+10/+10 cm^{-1}. In the averaged DDS the $C_4{=}O$ mode is upshifted 5/9/10 cm^{-1} (Fig. 7C, F, I), respectively. Therefore, it does not appear to be the case from a consideration of the calculated $C_4{=}O$ double difference band whether the averaged calculated DDS is more in line with the experimental DDS than the DDS calculated using the flipped or non-flipped models.

The experimental DDS in Fig. 4 suggest a PhQ^- band at 1476 cm^{-1}. The calculated DDS in Fig. 5 also display a weak negative band at 1476 cm^{-1} that is calculated to be due in part to a $C_4{=}O$ mode (see the movie titled "1476 mode of PhQ^-" in the SI).

The calculation for PhQ^- in Fig. 5A indicates very weak bands at 1517 and 1459 cm^{-1}. The 1517 cm^{-1} mode is due to a $\nu(C_2{=}C_3)$ in combination with a δ(CH) vibration, while the 1459 cm^{-1} mode is mainly a δ(CH) vibration (see movie titled "1517 and 1459 mode of PhQ^-" in the SI). These bands are hardly observable in the calculated DDS in Fig. 6. These two modes, however, may give rise to the negative bands at ~1520 and ~1456 cm^{-1} in the experimental FTIR DDS (Fig. 4).

For $DMNQ^-$ an intense $C_1{=}O$ mode is calculated at 1494 cm^{-1} (Fig. 5B), virtually the same as that for PhQ^-. The similarity in the calculated frequency, if translated to experiment, would predict no feature near 1495 cm^{-1} in the (DMNQ – PhQ) DDS. Such a prediction is in line with the experimental DDS (Fig. 4A).

For $DMNQ^-$, however, a predominantly $C_4{=}O$ mode is calculated at 1434 cm^{-1} (Fig. 5B) upshifted 6 cm^{-1} relative to the corresponding mode of PhQ^-. Experimentally, the upshift is ~11 cm^{-1} (Fig. 4A), so the correct trend is predicted but the magnitude of the calculated shift is considerably smaller than that observed.

For $2MNQ^-$, an intense mode is calculated at 1502/1505 cm^{-1} for non-flipped/flipped $2MNQ^-$, respectively (Fig. 5C). This mode is also predominantly due to a $C_1{=}O$ vibration (with some contribution from CH bending vibrations). This mode is upshifted 7-9 cm^{-1} relative to that of PhQ^- which is comparable with the 10 cm^{-1} observed experimentally.

For $2MNQ^-$ an intense mode is also calculated at ~1435 cm^{-1} for both flipped and non-flopped $2MNQ^-$ (Fig. 5C, 6B, 7A-C) and is primarily due to a $C_4{=}O$ vibration. This mode is upshifted 7 cm^{-1} relative to the corresponding PhQ^- mode. Experimentally an upshift of 15 cm^{-1} is observed. So, again, although the calculations correctly indicate the trend, the magnitude of the calculated shift is considerably smaller than that observed experimentally.

For $2MNQ^-$ the calculated separation between the $C_1{=}O$ and $C_4{=}O$ modes is ~67 cm^{-1}, close to the experimentally observed 75 cm^{-1}.

For $2ClNQ^-$, an intense mode is calculated at 1512 cm^{-1} (Fig. 5D). This mode is predominantly due to a $C_1{=}O$ vibration with weaker contributions from $C_4{=}O$, $C_2 = C_3$ stretching and CH bending vibrations. This mode is upshifted +17 cm^{-1} relative to the corresponding mode of PhQ^- and is also considerably more intense than the corresponding PhQ^- mode. Both the magnitude of the upshift and the intensity increase are in line with experiment.

For flipped $2ClNQ^-$ the $C_1{=}O$ vibration still upshifts to 1507 cm^{-1} (Fig. 5D). In the averaged of the two DDS two peaks are observed at 1511 and 1508 cm^{-1} (Fig. 7F). In the experimental DDS a positive band is observed at 1509 with a clear shoulder near 1500 cm^{-1} (Fig. 4C). These two peaks observed experimentally, along with the two peaks in the calculated average DDS suggest that 2ClNQ may adopt two orientations in the A_1 binding site. Given the higher intensity of the higher frequency component in the experimental DDS (at 1509 cm^{-1}) and taking into account that the higher frequency mode is calculated using a non-flipped model, the likelihood is

that non-flipped 2ClNQ is somewhat favored in the A_1 binding site. In summary, 2ClNQ can adopt two different conformations in the A_1 binding site, perhaps slightly favoring a conformation where the Cl atom is adjacent to the C_1=O group (meta to the H-bonded C_4=O group), as shown in the inset in Fig. 5. The (2BrNQ – PhQ) and (2BrNQ – PhQ) DDS are very similar. So, the same conclusions also apply to 2BrNQ incorporated into PSI.

For $2ClNQ^-$ a mode is calculated at 1429 cm^{-1} and is primarily due to a $C_4{=}O$ vibration. This mode is upshifted only 1 cm^{-1} relative to the corresponding mode of PhQ^-. This suggests that these features would cancel in a calculated DDS. Given that the PhQ^- mode has a higher intensity (compare Fig.5 A and D) a negative feature is observed near 1430 cm^{-1} in the calculated DDS (Fig. 6C). In the experimental (2ClNQ – PhQ) DDS (Fig. 4C) one hypothesis is that the negative band at 1414 cm^{-1} corresponds to the weak positive band at 1426 cm^{-1}. This 12 cm^{-1} upshift is considerably larger than the 1 cm^{-1} suggested by calculation. It may be the case that the negative 1414 cm^{-1} band corresponds to the positive band at 1442 cm^{-1} in Fig. 4C, so the upshift would be 28 cm^{-1}, even more at odds with the calculated data.

Very interestingly, the calculated spectra for the flipped 2ClNQ model shows a single band at 1439 cm^{-1}. However, this band is due to a predominantly C_2=C_3 vibration. The $C_4{=}O$ vibration appears near 1433 cm^{-1} but it is now much lower in intensity (Table S3).

Again, given the fact that the calculations indicate a $C_4{=}O$ mode of PhQ^- at 1428 cm^{-1} and not 1414 cm^{-1} is likely to pose problems in any calculation of DDS, and it is probably best to hold off on a detailed analysis of the DDS until more detailed QM/MM calculations have been undertaken.

For $2ClNQ^-$ bands are also calculated at 1461 and 1437 cm^{-1} (Fig. 5C). The origin of these bands are listed in Table S3 but it is not clear how they may relate to experiment. Again, more detailed QM/MM type models may better simulate these aspects of the experimental spectra. Calculated spectra and assignments for $2BrNQ^-$ are similar to that found and discussed for $2ClNQ^-$. This calculated similarity is also found experimentally.

Calculations for Cl_2 and Br_2NQ^- yield very similar results. There is also a high degree of similarity in the experimental DDS. Below we will discuss Cl_2NQ but recognize a similar discussion also follows for Br_2NQ.

For Cl_2NQ^- and Br_2NQ^- an intense vibrational mode calculated at 1505 cm^{-1} and 1501 cm^{-1}, respectively (Fig. 5F and G) and is largely due to an antisymmetric coupled $C{=}O$ vibration (with

weak contributions from aromatic CH bending and $C_2 = C_3$ stretching modes) (Table S3). So, the $C{=\!=}O$ mode of Cl_2NQ^- and Br_2NQ^- is calculated to be upshifted 6-10 cm^{-1} relative to the corresponding mode of PhQ^-, similar to that for $2MNQ^-$ and 7 cm^{-1} lower than that for $2ClNQ^-$ and $2BrNQ^-$. This ordering in the frequency of the modes for the different quinones is the same as that observed experimentally. Experimentally the frequency of the $C{=\!=}O$ mode in the (Cl_2NQ^- – PhQ^-) DDS is difficult to discern exactly but it is likely around 1505 cm^{-1} (Fig. 4E).

For Cl_2NQ^-, a vibrational mode is calculated at 1441 cm^{-1} (Fig. 6F) and is mainly a $C_4{=\!=}O$ vibration (with contributions from aromatic CH bending vibrations). So, for Cl_2NQ^- the $C_1{=\!=}O$ and $C_4{=\!=}O$ vibrational modes are calculated to be separated by 64 cm^{-1}. However, this putative $C_4{=\!=}O$ vibration is extremely weak compared to the antisymmetric coupled $C{=\!=}O$ vibration, and the calculations suggest that essentially a single $C{=\!=}O$ mode should be easily observed. This calculated prediction could be in line with experiment given the very weak positive band observed at 1426 cm^{-1} in Fig. 4 E,F, which may or may not be due to a $C_4{=\!=}O$ vibration.

This type of behavior, where only a single antisymmetric $C{=\!=}O$ vibration is observed experimentally [29] (and computationally [57, 62, 63]) for a bound semiquinone anion is reminiscent of the situation for plastoquinone (PQ) in the Q_A binding site in PSII. Off course, bound PQ in PSII is an asymmetrically substituted benzoquinone (BQ) in a somewhat symmetric H-bonding environment, and here we have a symmetrically substituted NQ (Cl_2NQ or Br_2NQ) in a distinctly asymmetric H–bonding environment. A more detailed QM/MM analysis of both Cl_2NQ in the A_1 binding site and PQ in the Q_A binding site is required.

Computationally, for $2ClNQ^-$ and $2BrNQ^-$ a pair of bands is calculated at 1437 and 1429 cm^{-1}. However, for Cl_2NQ^- and Br_2NQ^- a single band is calculated at 1441 cm^{-1}. This set of features does appear to be preserved in the experimental DDS, where a broad set of positive features is observed with peaks at 1442 and 1426 cm^{-1} in (2ClNQ – PhQ) and (2BrNQ – PhQ) DDS and a predominantly single feature at 1445 cm^{-1} is observed in (Cl_2NQ – PhQ) and (Br_2NQ – PhQ) DDS. This comparison/agreement between calculated and experimental features in four different DDS suggests some validity to the computational approach and the associated calculated normal mode compositions. It is worth noting that such features might also be suggested in calculations using the simpler models, except the two clear bands at 1437 and 1429 cm^{-1} in Fig. 5D, E merge into a single broad feature near 1438 cm^{-1} when the (Q^-+H_2O) model is used (Fig. S2).

5 CONCLUSIONS

Here we present time resolved FTIR DS and DDS obtained using PSI samples with a series of halogenated NQs incorporated. Comparing these DS and DDS to other previously published DDS, and also by considering corresponding calculated DDS we were able to assess the normal modes of the halogenated NQs in PSI, and from that make inferences on the orientation of the incorporated monosubstituted halogenated NQs in the A_1 binding site.

In this study, we identified two new bands for PhQ^- in the anion region (~1520 and ~1456 cm^{-1}). We also identified several bands for the incorporated halogenated NQs for the first time.

For the two mono-substituted halogenated NQs, $2ClNQ^-$/$2BrNQ^-$, the $C_1{=}O$ vibrational mode appears to contain contributions from two species, which via calculation we suggest is two different orientations for the incorporated NQs. Thus, the Cl or Br atom of the mono-substituted NQs appears not to have a specific preference for being meta or ortho to the H bonded C=O group.

For PSI with all the five NQs (PhQ^-, $DMNQ^-$, $2MNQ^-$, $2ClNQ^-$, $2BrNQ^-$, Br_2NQ^-) incorporated the frequency and intensity of the $C_1{=}O$ mode follows the same pattern in both the experimental and calculated spectra.

From the anion state, it was observed that $C_1{=}O$ and $C_4{=}O$ modes are separated by ~ 76 (±7 cm^{-1}) for all the five NQs which is reduced to ~63 (±3 cm^{-1}) for the two di-substituted halogenated NQs. For neutral PhQ in PSI the $C_1{=}O$ and $C_4{=}O$ modes are separated by ~30 cm^{-1}. The reduced frequency separation might indicate that the H-bonding is stronger in the anion state.

Declaration of competing interest

The authors declare that they have no known competing financial interests or personal relationships that could have appeared to influence the work reported in this paper.

6 ACKNOWLEDGEMENTS

This material is based upon work supported by the U.S. Department of Energy, Office of Science, Office of Basic Energy Sciences, under Award Number DE–SC–0017937 to GH. The statements made herein are solely the responsibility of the authors. NA acknowledges a fellowship from the Molecular Basis of Disease Program at Georgia State University.

7 REFERENCES

1. Walker, D., *Energy, plants and man*. 2nd ed., with amendments. ed. 1993, Brighton, East Sussex: University Science Books.
2. Nelson, N. and C.F. Yocum, *Structure and Function of Photosystems I and II.* Annual Review of Plant Biology, 2006. **57**(1): p. 521-565.
3. Nelson, N. and A. Ben-Shem, *The complex architecture of oxygenic photosynthesis.* Nat Rev Mol Cell Biol, 2004. **5**(12): p. 971-982.
4. Fromme, P., P. Jordan, and N. Krauss, *Structure of photosystem I.* Biochimica et Biophysica Acta (BBA) - Bioenergetics, 2001. **1507**(1-3): p. 5-31.
5. Jordan, P., et al., *Three-dimensional structure of cyanobacterial photosystem I at 2.5A resolution.* Nature, 2001. **411**(6840): p. 909-917.
6. Hastings, G., et al., *Universality of Energy and Electron Transfer Processes in Photosystem I.* Biochemistry, 1995. **34**(47): p. 15512-15522.
7. Hastings, G., et al., *Observation of the Reduction and Reoxidation of the Primary Electron Acceptor in Photosystem I.* Biochemistry, 1994. **33**(11): p. 3193-3200.
8. Guergova-Kuras, M., et al., *Evidence for two active branches for electron transfer in photosystem I.* Proceedings of the National Academy of Sciences, 2001. **98**(8): p. 4437-4442.
9. Agalarov, R. and K. Brettel, *Temperature dependence of biphasic forward electron transfer from the phylloquinone(s) A1 in photosystem I: only the slower phase is activated.* Biochimica et Biophysica Acta (BBA) - Bioenergetics, 2003. **1604**(1): p. 7-12.
10. Byrdin, M., et al., *Assignment of a kinetic component to electron transfer between iron–sulfur clusters FX and FA/B of Photosystem I.* Biochimica et Biophysica Acta (BBA) - Bioenergetics, 2006. **1757**(11): p. 1529-1538.
11. Shinkarev, V.P., et al., *Modeling of the P700+ Charge Recombination Kinetics with Phylloquinone and Plastoquinone-9 in the A1 Site of Photosystem I.* Biophysical Journal, 2002. **83**(6): p. 2885-2897.
12. Jordan, R., U. Nessau, and E. Schlodder, *Charge Recombination Between the Reduced Iron-Sulphur Clusters and P700+*, in *Photosynthesis: Mechanisms and Effects*, G. Garab, Editor. 1998, Springer Netherlands. p. 663-666.
13. Brettel, K., *Electron transfer and arrangement of the redox cofactors in photosystem I.* Biochimica et Biophysica Acta (BBA) - Bioenergetics, 1997. **1318**(3): p. 322-373.
14. Vassiliev, I.R., et al., *Near-IR absorbance changes and electrogenic reactions in the microsecond-to-second time domain in Photosystem I.* Biophysical Journal, 1997. **72**(1): p. 301-315.
15. Moser, C. and P.L. Dutton, *Application of Marcus Theory to Photosystem I Electron Transfer*, in *Photosystem I*, J. Golbeck, Editor. 2006, Springer Netherlands. p. 583-594.
16. Makita, H. and G. Hastings, *Modeling electron transfer in photosystem I.* Biochimica et Biophysica Acta (BBA) - Bioenergetics, 2016. **1857**(6): p. 723-733.
17. Schlodder, E., et al., *Temperature dependence of forward and reverse electron transfer from A1-, the reduced secondary electron acceptor in photosystem I.* Biochemistry, 1998. **37**(26): p. 9466-76.
18. Makita, H. and G. Hastings, *Directionality of electron transfer in cyanobacterial photosystem I at 298 and 77 K.* FEBS Letters, 2015. **589**(13): p. 1412-1417.
19. Redding, K., A. van der Est, and J.H. Golbeck, *The Directionality of Electron Transport in Photosystem I: Photosystem I*. 2006, Springer Netherlands. p. 413-437.
20. Makita, H., N. Zhao, and G. Hastings, *Time-resolved visible and infrared difference spectroscopy for the study of photosystem I with different quinones incorporated into the A1 binding site.* Biochimica et Biophysica Acta (BBA) - Bioenergetics, 2015. **1847**(3): p. 343-354.
21. Wang, J., et al., *Structure of plant photosystem I–light harvesting complex I supercomplex at 2.4 Å resolution.* 2021. **63**(7): p. 1367-1381.

22. Pi, X., et al., *Unique organization of photosystem I–light-harvesting supercomplex revealed by cryo-EM from a red alga.* 2018. **115**(17): p. 4423-4428.
23. Busch, A. and M.J.B.e.B.A.-B. Hippler, *The structure and function of eukaryotic photosystem I.* 2011. **1807**(8): p. 864-877.
24. Ben-Shem, A., F. Frolow, and N.J.N. Nelson, *Crystal structure of plant photosystem I.* 2003. **426**(6967): p. 630-635.
25. Pushkar, Y.N., et al., *Asymmetric Hydrogen-Bonding of the Quinone Cofactor in Photosystem I Probed by 13C-Labeled Naphthoquinones.* The Journal of Physical Chemistry B, 2004. **108**(27): p. 9439-9448.
26. Makita, H., et al., *Quinones in the A1 binding site in photosystem I studied using time-resolved FTIR difference spectroscopy.* Biochimica et Biophysica Acta (BBA) - Bioenergetics, 2017. **1858**(9): p. 804-813.
27. Srinivasan, N. and J.H. Golbeck, *Protein–cofactor interactions in bioenergetic complexes: The role of the A1A and A1B phylloquinones in Photosystem I.* Biochimica et Biophysica Acta (BBA) - Bioenergetics, 2009. **1787**(9): p. 1057-1088.
28. Johnson, T.W., et al., *Recruitment of a Foreign Quinone into the A1 Site of Photosystem I: I. Genetic and Physiological Characterization of Phylloquinone Biosynthetic Pathway Mutants in Synechocystis sp. PCC 6803.* Journal of Biological Chemistry, 2000. **275**(12): p. 8523-8530.
29. Makita, H. and G. Hastings, *Time-resolved step-scan FTIR difference spectroscopy for the study of photosystem I with different benzoquinones incorporated into the A1 binding site.* Biochimica et Biophysica Acta (BBA) - Bioenergetics, 2018. **1859**(11): p. 1199-1206.
30. Mula, S., et al., *Incorporation of a high potential quinone reveals that electron transfer in Photosystem I becomes highly asymmetric at low temperature.* Photochemical & Photobiological Sciences, 2012. **11**(6): p. 946-956.
31. van der Est, A., et al., *Incorporation of 2,3-Disubstituted-1,4-Naphthoquinones into the A1 Binding Site of Photosystem I Studied by EPR and ENDOR Spectroscopy.* Applied Magnetic Resonance, 2010. **37**(1-4): p. 65-83.
32. Makita, H. and G. Hastings, *Time-resolved visible and infrared absorption spectroscopy data obtained using photosystem I particles with non-native quinones incorporated into the A1 binding site.* Data in Brief, 2016. **7**: p. 1463-1468.
33. Johnson, T.W., et al., *Recruitment of a Foreign Quinone into the A1 Site of Photosystem I: in vivo Replacement of Plastoquinone-9 by Media-Supplemented Naphtoquinones in Phylloquinone Biosynthetic Pathway Mutants of Synechocystis sp. PCC 6803.* Journal of Biological Chemistry, 2001. **276**(43): p. 39512-39521.
34. Zybailov, B., et al., *Recruitment of a Foreign Quinone into the A1 Site of Photosystem I: II. Structural and Functional Characterization of Phylloquinone Biosynthetic Pathway Mutants by Electron Paramagnetic Resonance and Electron-Nuclear Double Resonance Spectroscopy.* Journal of Biological Chemistry, 2000. **275**(12): p. 8531-8539.
35. Mezzetti, A. and W. Leibl, *Time-resolved infrared spectroscopy in the study of photosynthetic systems.* Photosynthesis Research, 2016: p. 1-24.
36. Breton, J., et al., *Binding sites of quinones in photosynthetic bacterial reaction centers investigated by light-induced FTIR difference spectroscopy: Binding of chainless symmetrical quinones to the QA site of Rhodobacter sphaeroides.* Biochemistry, 1994. **33**(41): p. 12405-12415.
37. Hellwig, P., *Infrared spectroscopic markers of quinones in proteins from the respiratory chain.* Biochimica et Biophysica Acta (BBA) - Bioenergetics, 2015. **1847**(1): p. 126-133.
38. Makita, H. and G. Hastings, *Inverted-region electron transfer as a mechanism for enhancing photosynthetic solar energy conversion efficiency.* Proceedings of the National Academy of Sciences, 2017. **114**(35): p. 9267-9272.

39. Makita, H. and G. Hastings, *Time-resolved FTIR difference spectroscopy for the study of quinones in the A1 binding site in photosystem I: Identification of neutral state quinone bands.* Biochimica et Biophysica Acta (BBA) - Bioenergetics, 2020. **1861**(5): p. 148173.
40. Cyran, J.D., J.M. Nite, and A.T. Krummel, *Characterizing Anharmonic Vibrational Modes of Quinones with Two-Dimensional Infrared Spectroscopy.* The Journal of Physical Chemistry B, 2015. **119**(29): p. 8917-8925.
41. Sivakumar, V., R. Wang, and G. Hastings, *A1 Reduction in Intact Cyanobacterial Photosystem I Particles Studied by Time-Resolved Step-Scan Fourier Transform Infrared Difference Spectroscopy and Isotope Labeling†.* Biochemistry, 2005. **44**(6): p. 1880-1893.
42. Hastings, G., K.M. Priyangika Bandaranayake, and E. Carrion, *Time-Resolved FTIR Difference Spectroscopy in Combination with Specific Isotope Labeling for the Study of A1, the Secondary Electron Acceptor in Photosystem 1.* Biophysical Journal, 2008. **94**(11): p. 4383-4392.
43. Agarwala, N., et al., *Reversible inhibition and reactivation of electron transfer in photosystem I.* Photosynth Res, 2020.
44. Hastings, G., et al., *Fourier transform visible and infrared difference spectroscopy for the study of P700 in photosystem I from Fischerella thermalis PCC 7521 cells grown under white light and far-red light: Evidence that the A–1 cofactor is chlorophyll f.* Biochimica et Biophysica Acta (BBA) - Bioenergetics, 2019. **1860**(6): p. 452-460.
45. Wang, R., et al., *FTIR Difference Spectroscopy in Combination with Isotope Labeling for Identification of the Carbonyl Modes of P700 and P700+ in Photosystem I.* Biophysical Journal, 2004. **86**(2): p. 1061-73.
46. Snellenburg, J.J., et al., *Glotaran: a Java-based Graphical User Interface for the R-package TIMP.* Journal of Statistical Software, 2012. **49**(3): p. 1-22.
47. Agarwala, N., et al., *Calculated and Experimental Infrared Spectra of Substituted Naphthoquinones.* Frontiers in Science, Technology, Engineering and Mathematics (FSTEM), 2019. **3**(2): p. 71-80.
48. M. J. Frisch, G.W.T., H. B. Schlegel, G. E. Scuseria, M. A. Robb, J. R. Cheeseman, G. Scalmani, V. Barone, G. A. Petersson, H. Nakatsuji, X. Li, M. Caricato, A. Marenich, J. Bloino, B. G. Janesko, R. Gomperts, B. Mennucci, H. P. Hratchian, J. V. Ortiz, A. F. Izmaylov, J. L. Sonnenberg, D. Williams-Young, F. Ding, F. Lipparini, F. Egidi, J. Goings, B. Peng, A. Petrone, T. Henderson, D. Ranasinghe, V. G. Zakrzewski, J. Gao, N. Rega, G. Zheng, W. Liang, M. Hada, M. Ehara, K. Toyota, R. Fukuda, J. Hasegawa, M. Ishida, T. Nakajima, Y. Honda, O. Kitao, H. Nakai, T. Vreven, K. Throssell, J. A. Montgomery, Jr., J. E. Peralta, F. Ogliaro, M. Bearpark, J. J. Heyd, E. Brothers, K. N. Kudin, V. N. Staroverov, T. Keith, R. Kobayashi, J. Normand, K. Raghavachari, A. Rendell, J. C. Burant, S. S. Iyengar, J. Tomasi, M. Cossi, J. M. Millam, M. Klene, C. Adamo, R. Cammi, J. W. Ochterski, R. L. Martin, K. Morokuma, O. Farkas, J. B. Foresman, and D. J. Fox, *Gaussian 09, Revision D.01*. 2013, Gaussian, Inc., Wallingford CT, 2016.
49. Bandaranayake, K.M.P., et al., *Modeling the A(1) binding site in photosystem - I. Density functional theory for the calculation of "anion-neutral" FTIR difference spectra of phylloquinone.* Vibrational Spectroscopy, 2006. **42**(1): p. 78-87.
50. Tomasi, J., et al., *Molecular properties in solution described with a continuum solvation model.* 2002. **4**(23): p. 5697-5712.
51. Jamróz, M.H., *Vibrational Energy Distribution Analysis (VEDA): Scopes and limitations.* Spectrochimica Acta Part A: Molecular and Biomolecular Spectroscopy, 2013. **114**: p. 220-230.
52. Makita, H. and G. Hastings, *Photosystem I with benzoquinone analogues incorporated into the A1 binding site.* Photosynth Res, 2018. **137**(1): p. 85-93.
53. Rohani, L., et al., *Calculated vibrational properties of semiquinones in the A(1) binding site in photosystem I.* Biochim Biophys Acta Bioenerg, 2019. **1860**(9): p. 699-707.

54. Hastings, G., *Vibrational spectroscopy of photosystem I.* Biochim Biophys Acta, 2015. **1847**(1): p. 55-68.
55. Srinivasan, N., et al., *Role of the Hydrogen Bond from Leu722 to the A1A Phylloquinone in Photosystem I.* Biochemistry, 2009. **48**(15): p. 3315-3324.
56. Feldman, K.S., D.K. Hester Ii, and J.H. Golbeck, *A relationship between amide hydrogen bond strength and quinone reduction potential: Implications for photosystem I and bacterial reaction center quinone function.* Bioorganic & Medicinal Chemistry Letters, 2007. **17**(17): p. 4891-4894.
57. Ashizawa, R. and T. Noguchi, *Effects of hydrogen bonding interactions on the redox potential and molecular vibrations of plastoquinone as studied using density functional theory calculations.* Physical Chemistry Chemical Physics, 2014. **16**(24): p. 11864-11876.
58. Ivancich, A., et al., *Effects of hydrogen bonds on the redox potential and electronic structure of the bacterial primary electron donor.* Biochemistry, 1998. **37**(34): p. 11812-20.
59. Pushkar, Y.N., et al., *Orientation and Protein−Cofactor Interactions of Monosubstituted n-Alkyl Naphthoquinones in the A1 Binding Site of Photosystem I.* The Journal of Physical Chemistry B, 2002. **106**(46): p. 12052-12058.
60. Bandaranayake, K., R. Wang, and G. Hastings, *Modification of the Phylloquinone in the A_1 Binding Site in Photosystem I Studied Using Time-Resolved FTIR Difference Spectroscopy and Density Functional Theory.* Biochemistry, 2006. **45**(13): p. 4121-4127.
61. Rohani, L. and G. Hastings, *Assessment of the orientation and conformation of pigments in protein binding sites from infrared difference spectra.* Biochim Biophys Acta Bioenerg, 2021. **1862**(4): p. 148366.
62. Berthomieu, C., et al., *Characterization by FTIR spectroscopy of the photoreduction of the primary quinone acceptor QA in photosystem II.* FEBS Letters, 1990. **269**(2): p. 363-367.
63. Takano, A., et al., *Herbicide effect on the hydrogen-bonding interaction of the primary quinone electron acceptor QA in photosystem II as studied by Fourier transform infrared spectroscopy.* Photosynthesis Research, 2008. **98**(1): p. 159-167.